Mechanochemical formation of heterogeneous diamond structures during rapid uniaxial compression in graphite

Matthew P. Kroonblawd* and Nir Goldman
Physical and Life Sciences Directorate, Lawrence Livermore National Laboratory, Livermore, California 94550, United States

(Received 21 September 2017; published 25 May 2018)

We predict mechanochemical formation of heterogeneous diamond structures from rapid uniaxial compression in graphite using quantum molecular dynamics simulations. Ensembles of simulations reveal the formation of different diamondlike products starting from thermal graphite crystal configurations. We identify distinct classes of final products with characteristic probabilities of formation, stress states, and electrical properties and show through simulations of rapid quenching that these products are nominally stable and can be recovered at room temperature and pressure. Some of the diamond products exhibit significant disorder and partial closure of the energy gap between the highest-occupied and lowest-unoccupied molecular orbitals (i.e., the HOMO-LUMO gap). Seeding atomic vacancies in graphite significantly biases toward forming products with small HOMO-LUMO gap. We show that a strong correlation between the HOMO-LUMO gap and disorder in tetrahedral bonding configurations informs which kinds of structural defects are associated with gap closure. The rapid diffusionless transformation of graphite is found to lock vacancy defects into the final diamond structure, resulting in configurations that prevent sp^3 bonding and lead to localized HOMO and LUMO states with a small gap.

DOI: 10.1103/PhysRevB.97.184106

I. INTRODUCTION

The scientific and technological relevance of carbon allotropes has driven substantial interest [1–18] in the carbon phase diagram since the first laboratory-grown diamonds were reproducibly synthesized [19] in the 1950s. A detailed understanding of carbon phase boundaries and transformations is necessary for astrophysical models of planetary interiors [18,20,21] and white dwarfs [22], for the design of inertial confinement fusion targets [23], and for increased control in diamond manufacturing [24]. Recent efforts to tailor diamond on the nanoscale seek to produce components for photonics, electronics, and quantum computing [24–27]. Manufactured diamonds are commonly synthesized from carbon-containing precursors through chemical-vapor deposition [24,25,27] or under static high pressure and high temperature [19,24,28]. Another promising synthetic route is through direct mechanochemical transformation of graphite to diamond under uniaxial compression at very high strain rates (e.g., through shock compression) [1,3,4,12,15,17,18]. Atomic-level shear strains can prompt chemical reactions through mechanical means [29,30], which can be induced by highly nonhydrostatic stresses during uniaxial shock compression [31] and also through industrial processes such as ball milling [32] or by precision manipulation using atomic force microscopy [33]. Products obtained through mechanochemistry can differ from their thermally synthesized counterparts through the formation of long-lived metastable states [13,29]. We show that subjecting graphite to extremely rapid uniaxial strain rates can yield a means to synthesize diamondlike structures with characteristic probabilities of formation, stress states, and electrical properties.

Understanding materials synthesis in the laboratory can require investigating a great number of permutations of different starting materials and thermodynamic conditions, which are too costly to address with experimental trial and error alone. In addition, experiments tend to yield equations of state or spectra that can be difficult to interpret in terms of specific chemical reactivity. Quantum-based simulation methods such as density functional theory (DFT) [34] are often used to accurately model physical and chemical changes in materials progressing through the range of states visited during a shock on atomistic scales [12,35–38]. However, DFT molecular dynamics simulations require immense computational effort per simulation time step that can consequently impose harsh limits on the system sizes and timescales that can be studied. The density functional tight-binding method (DFTB) holds promise to approach DFT-level accuracy over a wide range of phases and states [37,39,40] while affording up to a thousandfold reduction in computational expense [41,42]. DFTB simultaneously yields information on electronic states and can provide significantly improved transferability over empirical molecular dynamics potentials [43–45], which tend to be inaccurate outside of their fitted regime. The relatively high throughput of DFTB allows for gathering ensemble statistics from numerous independent simulations run for a specific set of conditions. Probabilistic physics-based predictions such as these can inform the interpretation of noisy experimental results, validate the predictions of empirical potentials, and are also relevant considering that some continuum material models [46] take probability functions as input. Here, we use an established DFTB model for carbon under extreme conditions [37] with dispersion interactions [39] to investigate the ensemble-average response for the mechanochemical transformation of graphite to diamond under these dynamic loading conditions.

*kroonblawd1@llnl.gov

II. METHODS

Molecular dynamics simulations were performed using the DFTB method without self-consistent charges [47], similar to previous studies on carbon [37,39]. The total energy is defined as

$$E_{\text{Total}} = E_{\text{BS}} + E_{\text{Rep}} + E_{\text{Disp}}, \tag{1}$$

where E_{BS} is the band structure energy, E_{Rep} is a pairwise potential that is fit to reproduce ionic repulsion and Kohn-Sham double-counting terms, and E_{Disp} is a pairwise dispersion term. The band structure energy was evaluated using a minimal basis set with the pbc-0-3 parameter set [48]. Evaluations of E_{BS} were performed only at the Γ point without spin polarization and with Fermi-Dirac thermal smearing [49] with the electronic temperature set equal to the instantaneous ionic kinetic temperature at each time step. We used an E_{Rep} potential that was specifically developed [37] to model solid and liquid phases of carbon at extreme pressures and temperatures. An additional dispersion correction E_{Disp} was included that was originally parameterized [39] to better reproduce the experimental [50] compression curve and bulk modulus for graphite.

Trajectories were integrated using LAMMPS [51] with forces and stresses evaluated by the DFTB+ code [52]. Orthorhombic, three-dimensionally periodic simulation cells were used for all simulations. Isothermal-isochoric (NVT) and isothermal-isobaric (NPT) simulations were performed using a Nosé-Hoover-style thermostat and combined thermostat/barostat, respectively [53–55]. The three cell parameters were independently coupled to their respective diagonal stress tensor components in the NPT simulations. Isothermal simulations at $T = 300$ K were performed with a 0.50-fs time step, and all others were performed with a 0.25-fs time step.

A starting hexagonal graphite configuration with 288 atoms and six crystal layers was generated using the generalized crystal-cutting method [56] and the $T = 0$ K lattice parameters reported in Ref. [39]. The direction normal to the basal plane was aligned along z, and the corresponding cell dimension was 19.845 Å. The transverse cell directions were aligned in the x-y plane and had dimensions 12.471 $\times$9.600 Å^2. Simulations with larger system sizes using either a newly parallelized version of the DFTB+ code or recently developed classical force fields [57] are the subject of ongoing work. Average cell parameters were obtained at $T = 300$ K and $P = 1$ atm from the last 5 ps of a 10-ps NPT trajectory and were used to define the cell dimensions in subsequent simulations. Thirty thermal phase-space configurations were extracted in 1-ps intervals from the last 30 ps of a 50-ps NVT simulation performed at $T = 300$ K. These thermal configurations were used as independent starting points for compression simulations.

The DOLLS algorithm [58] was used to adiabatically compress the cell along z at a constant strain rate,

$$\dot{\epsilon} = \left| \frac{\Delta z}{z_0 \Delta t} \right|, \tag{2}$$

where Δz is the change in cell length from its initial value z_0 and Δt is the time interval for the compression. Simulation with DOLLS allows us to test for the possible dependence of mechanochemistry on the strain rate itself. This is in contrast to direct simulation of a shock compression (e.g., Ref. [59]), which would explicitly restrict our simulations to only a specific Rayleigh line. The initial density was $\rho_0 = 2.418$ g cm^{-3}. We set Δz to yield a final density $\rho_{\text{f}} = 3.925$ g cm^{-3}, which corresponds to a hydrostatic pressure of 50 GPa according to an experimental equation of state for diamond [6]. Four different strain rates ($\dot{\epsilon} = 1.0 \times 10^{11}, 5.0 \times 10^{10}, 1.0 \times 10^{10}$, and 5.0×10^9 s^{-1}) were considered, with corresponding Δt ranging from 3.8 to 76.8 ps. Average statistics for each postcompression state were obtained from a 5-ps isochoric-isoenergetic (NVE) trajectory following maximum compression.

Local bonding configurations were characterized using the atomic tetrahedral order parameter [60],

$$S_i = \frac{3}{32} \sum_{j=1}^{3} \sum_{k=j+1}^{4} \left(\hat{\mathbf{r}}_{ij} \cdot \hat{\mathbf{r}}_{ik} + \frac{1}{3} \right)^2 + \frac{1}{3} \sum_{j=1}^{4} \frac{(r_{ij} - \langle r \rangle)^2}{4 \langle r \rangle^2}, \tag{3}$$

where S_i is computed for central atom i, the sums run over the four nearest neighbors, $\hat{\mathbf{r}}_{ij}$ is the unit separation vector between atoms i and j, r_{ij} is the separation distance, and $\langle r \rangle$ is the arithmetic mean of r_{ij} computed for the four nearest neighbors. The first term in Eq. (3) measures the degree to which the four bond separation vectors are tetrahedrally aligned, and the second term is a measure of the variance in the bond lengths. Several relevant system averages $\langle S \rangle$ are 0.25 for an isotropic liquid, $\approx$0.20 for uncompressed graphite, and 0.00 for perfect diamond. Extended common-neighbor analysis [61] was used to identify cubic and hexagonal diamond packing. Standard common-neighbor analysis distinguishes between atoms in local fcc and hcp arrangements (among others) based on the bonding topology of neighboring atoms [62]. An extension of this analysis exploits the fact that cubic and hexagonal diamond structures consist of two intersecting lattices; a central atom in a local cubic- or hexagonal-diamond-packing environment has second-nearest neighbors that are respectively arranged on a fcc or hcp lattice. The Open Visualization Tool (OVITO) [63] was used to perform the extended common-neighbor analysis and render configuration snapshots.

The material stress state was characterized using scalar quantities proportional to the first and second rotational invariants of the stress tensor $\boldsymbol{\sigma}$, namely, the volumetric stress (or pressure, if hydrostatic) $P = \text{Tr}[\boldsymbol{\sigma}]/3$ and von Mises stress

$$\sigma_{\text{Mises}} = \frac{1}{\sqrt{2}} \big[(\sigma_{xx} - \sigma_{yy})^2 + (\sigma_{yy} - \sigma_{zz})^2 + (\sigma_{zz} - \sigma_{xx})^2 + 6 \big(\sigma_{xy}^2 + \sigma_{yz}^2 + \sigma_{zx}^2 \big) \big]^{1/2}. \tag{4}$$

The latter is a useful measure of deviatoric (shear) stress that is independent of coordinate frame. The average stress in the transverse dimensions was computed as $\sigma_{\text{Trans}} = (\sigma_{xx} + \sigma_{yy})/2$ for ease of comparison to the stress in the loading direction σ_{zz} as all three diagonal components of $\boldsymbol{\sigma}$ were, in general, unequal. We use the convention of positive stress for a compressed state. It should be noted that $\boldsymbol{\sigma}$ cannot be evaluated on a per-atom basis with the DFTB method (unlike many classical force fields), as E_{BS} in Eq. (1) is inherently many body and cannot be unambiguously reduced into contributions from interaction pairs.

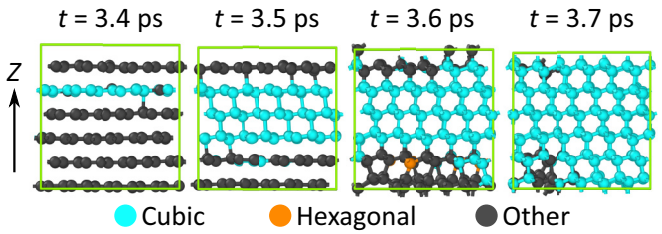

FIG. 1. Snapshots from a typical compression simulation showing the phase transformation from graphite to diamond. Atoms with local cubic- and hexagonal-diamond-packing environments identified by extended common-neighbor analysis are respectively colored cyan and orange. Other atoms that were not identified to have either diamond structure, such those in graphitic sheets, are colored black. The periodic simulation cell is drawn with green lines.

III. RESULTS

A. Compression response

We generated ensembles of 30 independent graphite compression simulations each for four different strain rates ($\dot{\epsilon} = 1.0 \times 10^{11}$, 5.0×10^{10}, 1.0×10^{10}, and 5.0×10^{9} s^{-1}), yielding a total of 120 statistically independent simulations. Strain rates were chosen to correspond to a broad range of possible experimental studies. Many of the qualitative features seen in our ensembles of simulations are generally consistent across the different simulations and strain rates, so we focus first on results from a single simulation at $\dot{\epsilon} = 1.0 \times 10^{11}$ s^{-1}. All simulations exhibit a rapid phase transformation from graphite to diamond. In the example simulation, the cell was compressed to its final density within 3.8 ps, and the phase transformation initiated at $t = 3.45$ ps. Snapshots of the simulation cell during the transformation are shown in Fig. 1. The transformation initiates with the buckling of a few graphite layers that form a layered diamond structure, similar to previous DFT results [12]. Neighboring layers quickly buckle thereafter until the entire structure transforms to a predominantly cubic diamond structure. The small region of atoms identified as "other" in the lower left-hand corner of the snapshot at $t = 3.7$ ps subsequently rearranges, leading to a cell that contains only perfect strained cubic diamond.

Time histories for the density, stress, kinetic temperature, and packing configuration are respectively shown in Figs. 2(a)–2(d) for a typical simulation. The onset of the phase transformation was identified by visual inspection of the trajectory, and the corresponding time is indicated in each panel. The phase transformation occurs after the system density exceeds the density of diamond at room temperature and pressure ($\rho_{\text{Diamond}} = 3.51$ g cm^{-3}). The absolute maximum in the stress along the compression direction σ_{zz} most clearly demarcates the time origin for the phase transformation. During the transformation, σ_{zz} rapidly decreases, while the transverse components σ_{Trans} rapidly increase. The volumetric stress remains approximately constant at ≈60 GPa during the transformation before finally reaching a value of 73 GPa at maximum compression. The temperature rise following the phase transformation is significantly greater (≈2000 K) than the initial ≈200 K increase due to work done to compress the graphite. The brief plateau in Fig. 2(d) at $t = 3.5$ ps

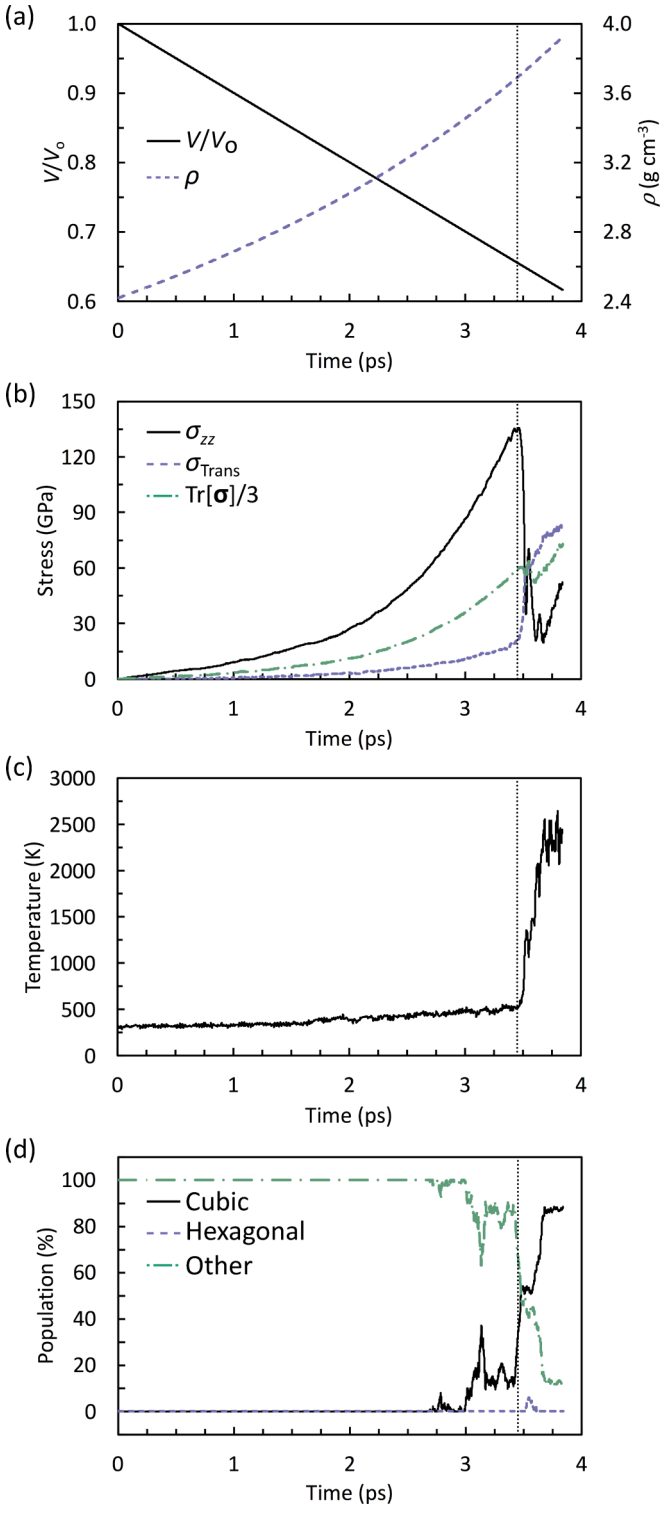

FIG. 2. Equation of state during a typical compression simulation showing (a) the volume and density, (b) the stress state, (c) the temperature, and (d) the population of atoms identified as either other or cubic/hexagonal diamond through extended common-neighbor analysis. Initiation of the phase transformation at 3.45 ps was identified through visual inspection of the trajectory (see Fig. 1) and is indicated by the vertical dotted line.

corresponds to the transient layered diamond configuration previously seen in Fig. 1, where only ≈50% of the atoms have

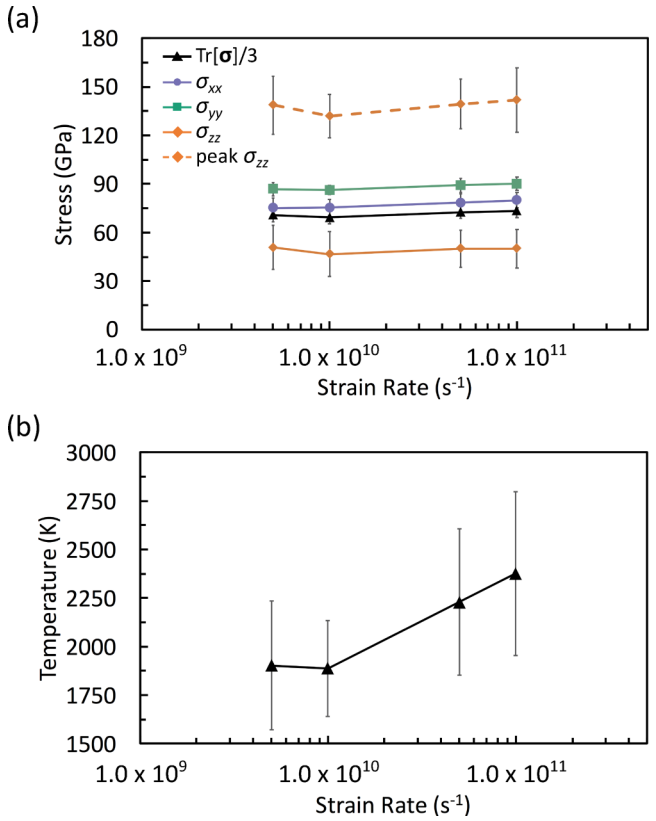

FIG. 3. Ensemble averages for the final (a) stress state and (b) temperature, plotted as a function of strain rate. Note that the ensemble averages for peak σ_{zz} were extracted from the compression portion of each trajectory, unlike the other plotted quantities. Error bars correspond to one standard deviation of the ensemble mean.

transformed to cubic diamond with the others remaining in graphitelike sheets. The fluctuations in relative population seen to the left of the dotted phase transformation could indicate an earlier transformation time origin than was identified by visual inspection of the trajectory. However, this analysis could be prone to error with the rapidly changing adaptive cutoff [64] used in the extended common-neighbor analysis [61]. The final configuration is not 100% cubic diamond due to the formation of a defect that subsequently anneals during the 5-ps postcompression NVE equilibration.

Possible strain rate dependence was investigated by comparing the ensemble-average response for selected compression rates in an interval spanning nearly two orders of magnitude. Average postcompression states were first determined for each trajectory using a 5-ps NVE simulation. These time averages were then used to compute the ensemble average for the final state, taking the ensemble standard deviation as the uncertainty. The final stress state and temperature are plotted as a function of strain rate in Figs. 3(a) and 3(b), respectively. Final stresses in the material are nonhydrostatic and independent of strain rate, with longitudinal and transverse stresses agreeing within the ensemble fluctuations for the slowest and fastest rates. The peak value for σ_{zz}, which we determined during each compression simulation, is also independent of the rate. The final temperature is only weakly dependent on strain rate within uncertainty, with $T_f = 2400 \pm 400$ K and $T_f = 1900 \pm 300$ K for the fastest and slowest cases. The decrease in T_f with decreasing rate is likely due to the smaller degree of irreversible work under those conditions.

Sufficiently fast strain rates could drive the system to a metastable density and temperature state for which the minimum-free-energy configuration would be diamond. We used the peak σ_{zz} to systematically define the time origin of the phase transformation (denoted by PT) and found the average density and von Mises stress at this point to be $\rho_{PT} = 3.70$ g cm^{-3} and $\sigma_{Mises,PT} = 127$ GPa, respectively. Both ρ_{PT} and $\sigma_{Mises,PT}$ were independent of strain rate and had respective maximum ensemble standard deviations of 0.08 g cm^{-3} and 14 GPa. Clearly, for the present case the probability to initiate the phase transformation is highly dependent on the strain but not the strain rate. A likely explanation is that the rates explored here are all too fast for thermal activation of the transformation, which instead initiates through mechanochemistry. This is consistent with the constant maximum deviatoric stress $\sigma_{Mises,PT}$ that the graphite structure supports before transforming.

B. Diamond products

Structural properties for the diamond products from our simulations indicate that ≈47% of the simulations exhibited some sort of defect, consistent with earlier shock experiments on pyrolytic graphite [4]. Our observed distribution of products and defects was found to be independent of strain rate. We observe four different types of postcompression configurations that are predominantly cubic diamond (Fig. 4): those with *no defects*, those with *pure twins* (a mirror-plane defect), and those with either *local disorder* or *extended disorder* to the tetrahedral bonding coordination. The percentage of simulations resulting in each product type was determined from our ensembles, averaged over all strain rates (120 independent simulations total), and the resulting distribution is shown in Fig. 4(b). Local and extended disorder configurations were differentiated based on whether regions of nondiamondlike atoms extended through the periodic boundary. Two typical configurations classified as having local disorder are shown to illustrate different possible degrees of defect localization relative to the extended disorder type. Two different subtypes of extended disorder were identified, with some exhibiting twin defects and others without them. Practically all of the configurations with local disorder also exhibited regions with hexagonal diamond. The small minority of products (≈2%) exhibiting extended disorder without twins also exhibit a partial closure of the energy gap between the highest-occupied and lowest-unoccupied molecular orbitals (i.e., the HOMO-LUMO gap) to $E_{Gap} \approx 0.5$ eV. All other configurations exhibited a large E_{Gap} of approximately 4.3 eV, which is consistent with experiments [1] that shock compressed pyrolytic graphite to an electrically insulating diamondlike phase. We verified that the defect types shown in Fig. 4(a) were recoverable at $T = 300$ K and $\mathrm{Tr}[\boldsymbol{\sigma}]/3 = 1$ atm by performing NPT simulations of rapid quenching in which a linearly ramped thermostat and barostat were applied to take each system from the hot compressed state to ambient conditions over the course of 50 ps.

Histograms of the average postcompression stress state for systems with different types of defects [Fig. 4(c)] indicate that the transverse stresses σ_{xx} and σ_{yy} are modestly insensitive to

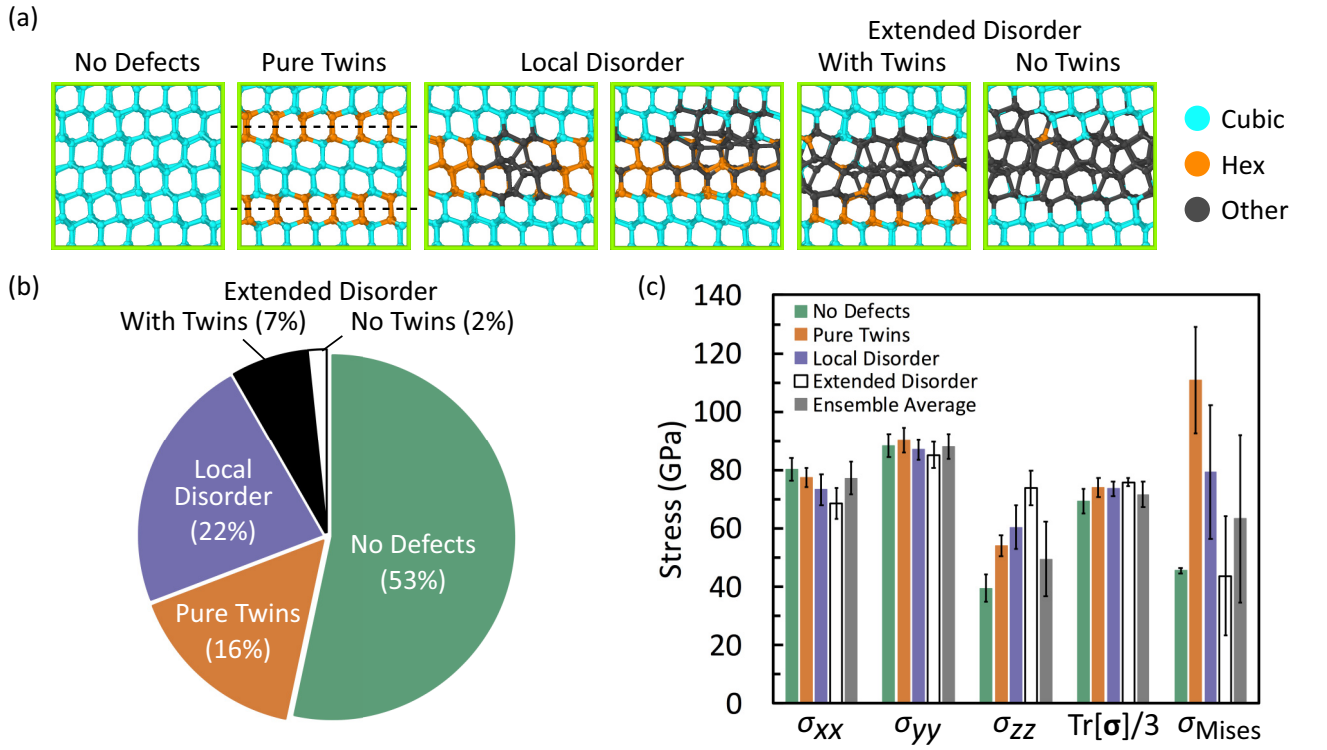

FIG. 4. (a) Typical persistent postcompression configurations with atoms colored by their local packing structure (cubic diamond, hexagonal diamond, or other). Dashed lines indicate twin mirror planes, and the simulation cell is drawn with solid green lines. Bonds are drawn using a 2-Å separation distance cutoff. (b) Population statistics for the different types of final products averaged over all strain rates. (c) Average postcompression stress states, with error bars corresponding to one standard deviation of the mean.

the presence or absence of defects, whereas the longitudinal stress σ_{zz} is much lower in systems without defects. The subtle variations in σ_{xx}, σ_{yy}, and σ_{zz} compensate to yield a total system pressure $\mathrm{Tr}[\boldsymbol{\sigma}]/3$ that is also independent of the defects. Specific defect types are predicted to have distinct signatures in the von Mises stress σ_{Mises}. Systems with twins exhibit the highest average σ_{Mises} of 111 GPa, which is slightly lower than the maximum (127 GPa) at the phase transformation. The σ_{Mises} stresses are predicted to relax with increasing disorder, with the local and extended disorder types yielding values of 79 and 44 GPa, respectively. The opposite trend appears to be true for σ_{zz}, where extended disorder configurations yielded the highest stress states. Nonzero shear stresses also manifest in the quenched products at ambient conditions, except for those instances that do not exhibit defects.

The defects observed in our simulations likely form due to an initial misalignment of the graphite layers that prevents a complete transformation to the ideal structure under extremely rapid compression rates. Example snapshots highlighting the phase transformation processes that ultimately yield diamond products with defects are shown in Fig. 5. Visual inspection of the trajectories reveals that pure twins arise when multiple layers initially buckle ($t = 0$ fs). These layers then bond to their neighbors, producing two layered diamond regions ($t = 30$ fs) that are aligned such that when the two regions meet, they form twins ($t \geqslant 60$ fs). Disordering arises due to layer misalignments that pin some atoms in a given layer (see extended disorder case at $t = 60$ and 90 fs), which prevents the overall alignment of that layer with the new lattice. This appears to be a consequence of the extremely rapid diffusionless transformation process. The extended disorder case exhibits greater layer misalignment at earlier times than the local disorder case does (compare snapshots at $t = 60$ fs). It is apparent from both disordered cases that initial misalignment and disordering can also be locked into the final structure when the cubic diamond region grows through the periodic boundary, which is analogous to the situation where two separate nucleation sites coalesce. Determining the spatial extent of extended disorder defects that develop in larger systems is the subject of future work.

Atomic vacancies present in real graphite crystals could potentially bias toward gap-closing defect structures in diamonds formed through uniaxial compression. Previous work has shown the ability to create highly specific extended defects and vacancies in graphite materials [65,66]. Thus, there exists the possibility to create materials with specific properties through mechanochemistry based on the initial defect structure of the system. In this respect, we considered four analogous 30-simulation ensembles at a strain rate of 1.0×10^{11} s^{-1}, starting from initial thermal graphite configurations with between one and four contiguous vacancies in a single crystal layer. These four vacancy systems correspond to defect concentrations of 0.35%, 0.69%, 1.04%, and 1.39%. Peak values for σ_{zz} and σ_{Mises} decrease from 142 to 122 GPa and from 127 to 111 GPa, respectively, going from zero to four vacancies. These reductions are consistent with the expectation that vacancies should

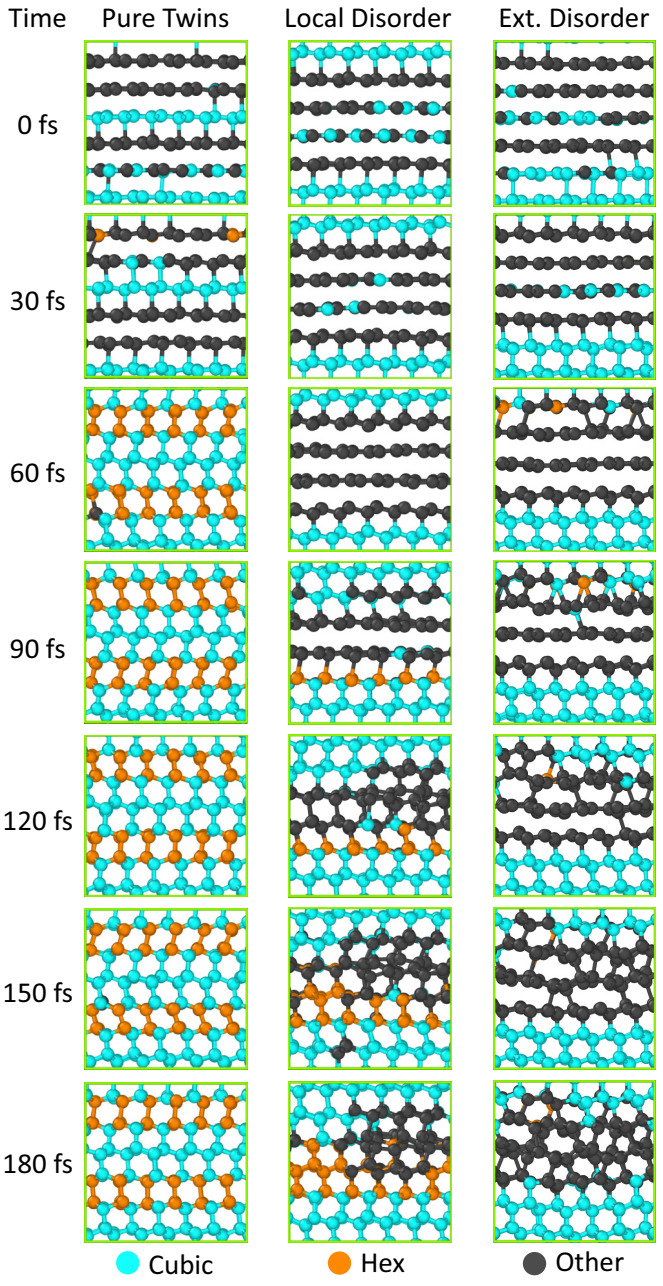

FIG. 5. Snapshots showing the kinds of transformation processes that lead to diamond products with pure twins, local disorder, and extended disorder. The time origin is set to the initiation of the phase transformation determined by the σ_{zz} criterion.

lower the free-energy barrier for the phase transformation. Final configurations obtained from the vacancy simulations fall into the same four categories as the initially defect free simulations (no defect, pure twins, local disorder, extended disorder), but with the additional presence of vacancies. The number of simulations that exhibit extended disorder increases by ≈10% when a single- or multicenter vacancy is introduced. Our results show that the locations of seeded vacancies are largely preserved during the diffusionless phase transformation, as the extremely rapid compression rates lock preexisting vacancies into the final structure. It is possible that slower

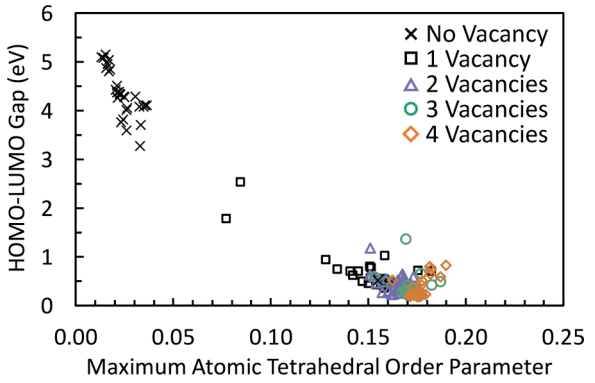

FIG. 6. Average E_{Gap} plotted as a function of the average maximum in the atomic tetrahedral order parameter for each simulation, where averages were computed over the 5-ps postcompression NVE trajectory portions. The single initially defect free (nonvacancy) simulation with partial gap closure corresponds to a configuration with extended disorder without twins.

compression rates might allow sufficient time for vacancy defects to anneal or migrate.

A correlation analysis between the HOMO-LUMO gap and the maximum in the tetrahedral order parameter S [see Eq. (3)] was computed for the ensembles of postcompression states and is shown in Fig. 6. A significant correlation between defects to the tetrahedral coordination of the final state (identified by $S > 0$) and partial closure of the HOMO-LUMO gap E_{Gap} was identified. Nearly all of the simulations with vacancies had some atoms in nontetrahedral bonding configurations. Other kinds of defects that do not perturb the bonding coordination, such as twins, do not strongly influence the electrical properties of the diamond products. In contrast to the initially defect free simulations, nearly all of those simulations that start with one or more vacancies exhibit $E_{\mathrm{Gap}} < 1$ eV. The ensemble average E_{Gap} decreases from 0.7 to 0.3 eV when the number of vacancies is increased from one to four. These gap closures are sufficient to result in partial occupation of the LUMO due to thermal excitation in the postcompression state and could affect electrical and thermal conductivity measurements. The correlation between nontetrahedral bonding coordination and gap closure suggests that mechanochemistry of rapidly compressed graphite with seeded vacancies could be a possible route to obtain diamondlike materials with significantly reduced E_{Gap}.

Density functional theory single-point calculations were performed for selected diamond structures to validate the DFTB-predicted HOMO-LUMO gap and obtain maps for the electronic density. Calculations were performed using the Vienna Ab initio Simulation Package (VASP) [67], using the Perdew-Burke-Ernzerhof [68] generalized gradient approximation functional with projector augmented-wave potentials [69,70]. The electronic structure was evaluated at only the Γ point using a 500 eV plane-wave cutoff without spin polarization and with Fermi-Dirac thermal smearing [49] with the electron temperature set to 0.215 eV (i.e., 2500 K, the approximate temperature of each compressed state). The self-consistent field accuracy threshold was set to 10^{-6} eV. Renderings of electronic density isosurfaces were prepared

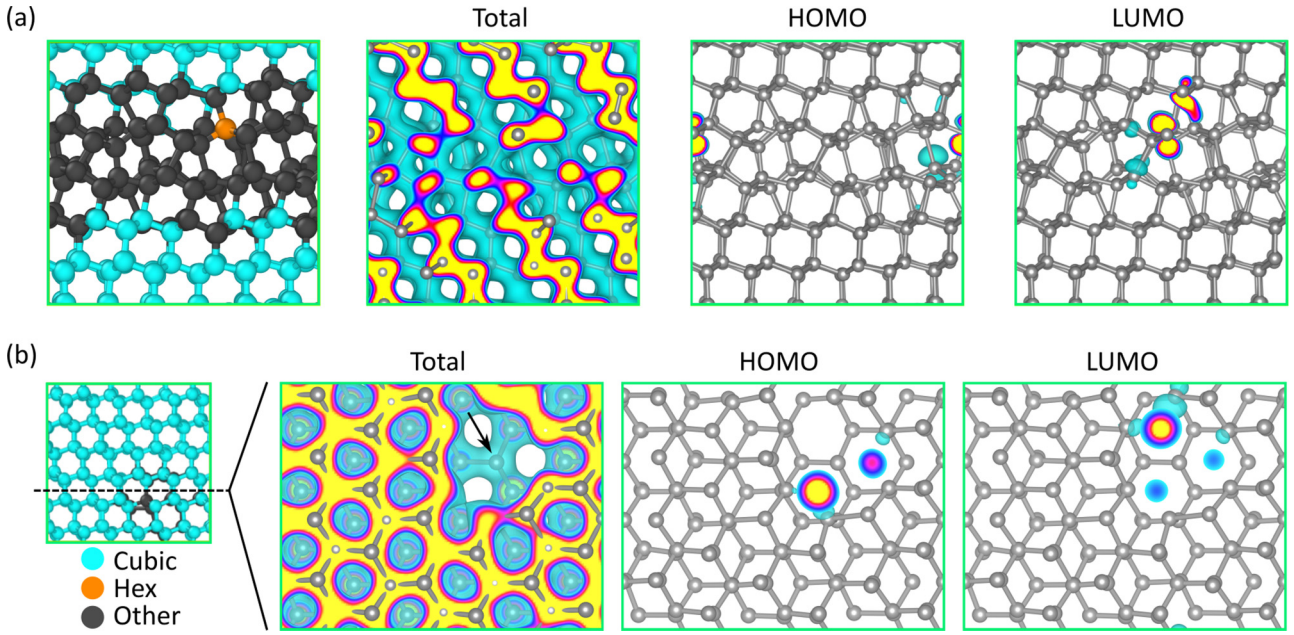

FIG. 7. Snapshots showing extended common-neighbor-analysis packing assignments and electronic density for two different diamond product types with a small HOMO-LUMO gap, including (a) an example with extended disorder without twins and (b) a predominantly cubic diamond structure obtained from compressed graphite seeded with four contiguous vacancies. Isosurfaces (cyan) are shown for the total electronic density and for the HOMO and LUMO states. The planar cross sections of the simulation cell shown here also reveal regions with higher density bounded by the isosurfaces that are indicated in blue, magenta, and yellow. Electronic density maps shown in (b) are oriented so that the normal vector for the slicing plane indicated in the far left snapshot is pointed out of the page.

using VESTA [71]. Figure 7 shows plots of the electronic density for two diamond products with small gap, including the extended disorder configuration without twins shown in Fig. 4 (rotated by 180°) and a typical example where a four-center vacancy is the only structural defect. The DFT-predicted E_{Gap} for these configurations are 0.31 and 0.13 eV, respectively, which are both close to the DFTB NVE averages of 0.51 and 0.05 eV plotted in Fig. 6. The extended disorder case exhibits HOMO and LUMO states that localize to separate and distinct parts of the disordered region (identified as "other" by the common-neighbor analysis). This disorder also correlates with irregularities in the covalent bonding network revealed by the total electron density. Due to the rapid diffusionless transformation, vacancies in graphite are locked into the final diamond structure and are clearly revealed by both the common-neighbor analysis and the total electron density. Atoms centered on the top and bottom of the vacancy cannot sp^3 bond to their neighbors and instead adopt pyramidal sp^2 configurations [see arrow in Fig. 7(b)]. Geometric constraints resulting in sp^2 configurations are a likely explanation for the consistent closure of the gap in the vacancy samples. The HOMO and LUMO states localize to the interior of the vacancy centered on the missing atomic sites and generally overlap, which might facilitate electronic transitions.

IV. CONCLUSIONS

Our DFTB model for carbon under extreme conditions allows for ensemble simulations of different strain pathways, which in turn yields a more realistic sampling of phase space than previous efforts. We found that use of independent thermal starting configurations can have a significant bearing on the distribution of final diamond products formed during the mechanochemical transformation of graphite. This is due to the fact that the instantaneous atomic configuration before compression dictates the end products observed in our simulations. Our results indicate that the rapid compressions studied here can induce defects and disordered structures in the diamond end product, which in some cases results in a partial closure of the material band gap. In particular, seeded vacancy sites in the graphite starting material can become "pinned" into specific geometries as the material is strained, allowing for small band gap energies where the HOMO and LUMO states are localized and centered within the vacancy site. Capturing the spectrum of nonideal products such as we have done here can inform the development and validation of coarse-grained material models and interpretation of experiments, especially considering the wide variation in possible structural, mechanical, and electrical properties of those products. Our results indicate the possibility of using mechanochemical synthetic routes to create materials with tailored properties, where desired characteristics are imparted as a direct result of the extremely rapid strain experienced by the material.

ACKNOWLEDGMENTS

The authors thank R. Lindsey and N. Mathew for useful discussions. This work was performed under the auspices of the U.S. Department of Energy by Lawrence Livermore National Laboratory under Contract No. DE-AC52-07NA27344.

[1] A. Mitchell, J. Shaner, and R. Keeler, Physica B+C (Amsterdam) **139**, 386 (1986).
[2] D. J. Erskine and W. J. Nellis, Nature (London) **349**, 317 (1991).
[3] H. Hirai and K.-I. Kondo, Science **253**, 772 (1991).
[4] D. J. Erskine and W. J. Nellis, J. Appl. Phys. **71**, 4882 (1992).
[5] S. Scandolo, M. Bernasconi, G. L. Chiarotti, P. Focher, and E. Tosatti, Phys. Rev. Lett. **74**, 4015 (1995).
[6] F. Occelli, P. Loubeyre, and R. LeToullec, Nat. Mater. **2**, 151 (2003).
[7] D. K. Bradley, J. H. Eggert, D. G. Hicks, P. M. Celliers, S. J. Moon, R. C. Cauble, and G. W. Collins, Phys. Rev. Lett. **93**, 195506 (2004).
[8] L. M. Ghiringhelli, J. H. Los, E. J. Meijer, A. Fasolino, and D. Frenkel, Phys. Rev. Lett. **94**, 145701 (2005).
[9] F. J. Ribeiro, P. Tangney, S. G. Louie, and M. L. Cohen, Phys. Rev. B **72**, 214109 (2005).
[10] A. A. Correa, S. A. Bonev, and G. Galli, Proc. Natl. Acad. Sci. U.S.A. **103**, 1204 (2006).
[11] M. D. Knudson, M. P. Desjarlais, and D. H. Dolan, Science **322**, 1822 (2008).
[12] C. J. Mundy, A. Curioni, N. Goldman, I.-F. W. Kuo, E. J. Reed, L. E. Fried, and M. Ianuzzi, J. Chem. Phys. **128**, 184701 (2008).
[13] J. Sun, D. D. Klug, and R. Martoňák, J. Chem. Phys. **130**, 194512 (2009).
[14] R. Z. Khaliullin, H. Eshet, T. D. Kühne, J. Behler, and M. Parrinello, Nat. Mater. **10**, 693 (2011).
[15] N. Pineau, J. Phys. Chem. C **117**, 12778 (2013).
[16] H. Xie, F. Yin, T. Yu, J.-T. Wang, and C. Liang, Sci. Rep. **4**, 5930 (2014).
[17] D. Kraus, A. Ravasio, M. Gauthier, D. O. Gericke, J. Vorberger, S. Frydrych, J. Helfrich, L. B. Fletcher, G. Schaumann, B. Nagler, B. Barbrel, B. Bachmann, E. J. Gamboa, S. Göde, E. Granados, G. Gregori, H. J. Lee, P. Neumayer, W. Schumaker, T. Döppner, R. W. Falcone, S. H. Glenzer, and M. Roth, Nat. Commun. **7**, 10970 (2016).
[18] D. Kraus, J. Vorberger, A. Pak, N. J. Hartley, L. B. Fletcher, S. Frydrych, E. Galtier, E. J. Gamboa, D. O. Gericke, S. H. Glenzer, E. Granados, M. J. MacDonald, A. J. MacKinnon, E. E. McBride, I. Nam, P. Neumayer, M. Roth, A. M. Saunders, A. K. Schuster, P. Sun, T. van Driel, T. Döppner, and R. W. Falcone, Nat. Astron. **1**, 606 (2017).
[19] F. P. Bundy, H. T. Hall, H. M. Strong, and R. H. Wentorf, Nature (London) **176**, 51 (1955).
[20] W. B. Hubbard, Science **214**, 145 (1981).
[21] S. Seager, M. Kuchner, C. A. Hier-Majumder, and B. Militzer, Astrophys. J. **669**, 1279 (2007).
[22] L. Segretain, G. Chabrier, M. Hernanz, E. Garcia-Berro, J. Isern, and R. Mochkovitch, Astrophys. J. **434**, 641 (1994).
[23] J. Biener, D. D. Ho, C. Wild, E. Woerner, M. M. Biener, B. S. El-dasher, D. G. Hicks, J. H. Eggert, P. M. Celliers, G. W. Collins, N. E. Teslich, Jr., B. J. Kozioziemski, S. W. Haan, and A. V. Hamza, Nucl. Fusion **49**, 112001 (2009).
[24] R. S. Balmer, J. R. Brandon, S. L. Clewes, H. K. Dhillon, J. M. Dodson, I. Friel, P. N. Inglis, T. D. Madgwick, M. L. Markham, T. P. Mollart, N. Perkins, G. A. Scarsbrook, D. J. Twitchen, A. J. Whitehead, J. J. Wilman, and S. M. Woollard, J. Phys. Condens. Matter **21**, 364221 (2009).
[25] I. Aharonovich, J. C. Lee, A. P. Magyar, B. B. Buckley, C. G. Yale, D. D. Awschalom, and E. L. Hu, Adv. Mater. **24**, OP54 (2012).
[26] M. J. Burek, N. P. de Leon, B. J. Shields, B. J. M. Hausmann, Y. Chu, Q. Quan, A. S. Zibrov, H. Park, M. D. Lukin, and M. Lončar, Nano Lett. **12**, 6084 (2012).
[27] I. Aharonovich, J. C. Lee, A. P. Magyar, D. O. Bracher, and E. L. Hu, Laser Photonics Rev. **7**, L61 (2013).
[28] A. Merlen, P. Toulemonde, S. L. Floch, G. Montagnac, T. Hammouda, O. Marty, and A. S. Miguel, Carbon **47**, 1643 (2009).
[29] J. J. Gilman, Science **274**, 65 (1996).
[30] T. Luty, P. Ordon, and C. J. Eckhardt, J. Chem. Phys. **117**, 1775 (2002).
[31] J. J. Gilman, Philos. Mag. B **71**, 1057 (1995).
[32] T. Friščić, I. Halasz, P. J. Beldon, A. M. Belenguer, F. Adams, S. A. J. Kimber, V. Honkimäki, and R. E. Dinnebier, Nat. Chem. **5**, 66 (2012).
[33] C. A. M. Seidel and R. Kuhnemuth, Nat. Nanotechnol. **9**, 164 (2014).
[34] W. Kohn and L. J. Sham, Phys. Rev. **140**, A1133 (1965).
[35] E. J. Reed, M. Riad Manaa, L. E. Fried, K. R. Glaesemann, and J. D. Joannopoulos, Nat. Phys. **4**, 72 (2007).
[36] N. Goldman, E. J. Reed, I.-F. W. Kuo, L. E. Fried, C. J. Mundy, and A. Curioni, J. Chem. Phys. **130**, 124517 (2009).
[37] N. Goldman and L. E. Fried, J. Phys. Chem. C **116**, 2198 (2011).
[38] K. Shimamura, M. Misawa, S. Ohmura, F. Shimojo, R. K. Kalia, A. Nakano, and P. Vashishta, Appl. Phys. Lett. **108**, 071901 (2016).
[39] C. B. Cannella and N. Goldman, J. Phys. Chem. C **119**, 21605 (2015).
[40] N. Goldman, Chem. Phys. Lett. **622**, 128 (2015).
[41] N. Goldman, S. G. Srinivasan, S. Hamel, L. E. Fried, M. Gaus, and M. Elstner, J. Phys. Chem. C **117**, 7885 (2013).
[42] S. G. Srinivasan, N. Goldman, I. Tamblyn, S. Hamel, and M. Gaus, J. Phys. Chem. A **118**, 5520 (2014).
[43] J. Tersoff, Phys. Rev. B **39**, 5566 (1989).
[44] D. W. Brenner, O. A. Shenderova, J. A. Harrison, S. J. Stuart, B. Ni, and S. B. Sinnott, J. Phys. Condens. Matter **14**, 783 (2002).
[45] J. H. Los and A. Fasolino, Phys. Rev. B **68**, 024107 (2003).
[46] M. R. Baer, D. K. Gartling, and P. E. DesJardin, Combust. Theor. Model. **16**, 75 (2012).
[47] D. Porezag, T. Frauenheim, T. Köhler, G. Seifert, and R. Kaschner, Phys. Rev. B **51**, 12947 (1995).
[48] The pbc-0-3 parameter set is available at https://www.dftb.org/.
[49] N. D. Mermin, Phys. Rev. **137**, A1441 (1965).
[50] M. Hanfland, H. Beister, and K. Syassen, Phys. Rev. B **39**, 12598 (1989).
[51] S. Plimpton, J. Comput. Phys. **117**, 1 (1995); LAMMPS is available at http://lammps.sandia.gov.
[52] B. Aradi, B. Hourahine, and T. Frauenheim, J. Phys. Chem. A **111**, 5678 (2007); DFTB+ is available at https://www.dftb-plus.info/.
[53] S. Nosé, J. Chem. Phys. **81**, 511 (1984).
[54] W. G. Hoover, Phys. Rev. A **31**, 1695 (1985).
[55] G. J. Martyna, D. J. Tobias, and M. L. Klein, J. Chem. Phys. **101**, 4177 (1994).
[56] M. P. Kroonblawd, N. Mathew, S. Jiang, and T. D. Sewell, Comput. Phys. Commun. **207**, 232 (2016).
[57] R. K. Lindsey, L. E. Fried, and N. Goldman, J. Chem. Theory Comput. **13**, 6222 (2017).
[58] W. G. Hoover, D. J. Evans, R. B. Hickman, A. J. C. Ladd, W. T. Ashurst, and B. Moran, Phys. Rev. A **22**, 1690 (1980).

[59] E. J. Reed, L. E. Fried, and J. D. Joannopoulos, Phys. Rev. Lett. **90**, 235503 (2003).
[60] P. L. Chau and A. J. Hardwick, Mol. Phys. **93**, 511 (2010).
[61] E. Maras, O. Trushin, A. Stukowski, T. Ala-Nissila, and H. Jónsson, Comput. Phys. Commun. **205**, 13 (2016).
[62] J. D. Honeycutt and H. C. Andersen, J. Phys. Chem. **91**, 4950 (1987).
[63] A. Stukowski, Model. Simul. Mater. Sci. Eng. **18**, 015012 (2010); OVITO is available at https://www.ovito.org.
[64] A. Stukowski, Model. Simul. Mater. Sci. Eng. **20**, 045021 (2012).
[65] K. Kim, H.-B.-R. Lee, R. W. Johnson, J. T. Tanskanen, N. Liu, M.-G. Kim, C. Pang, C. Ahn, S. F. Bent, and Z. Bao, Nat. Commun. **5**, 4781 (2014).
[66] T. Trevethan, C. D. Latham, M. I. Heggie, P. R. Briddon, and M. J. Rayson, Nanoscale **6**, 2978 (2014).
[67] G. Kresse and J. Furthmüller, Comput. Mater. Sci. **6**, 15 (1996).
[68] J. P. Perdew, K. Burke, and M. Ernzerhof, Phys. Rev. Lett. **77**, 3865 (1996).
[69] P. E. Blöchl, Phys. Rev. B **50**, 17953 (1994).
[70] G. Kresse and D. Joubert, Phys. Rev. B **59**, 1758 (1999).
[71] K. Momma and F. Izumi, J. Appl. Crystallogr. **44**, 1272 (2011).